Area specific resistance of in-situ oxidized Mn-Cu and Mn-Co metal powders as contact layers for the solid oxide cell air side

B. Talic [a,b,*], C. Goebel [a], I. Ritucci [a,c], Å.H. Persson [a], R. Kiebach [a], H.L. Frandsen [a]

[a] *Department of Energy Conversion and Storage, Technical University of Denmark, Anker Engelunds vej, KD-2800 Kgs., Lyngby, Denmark*
[b] *SINTEF Industry, Department of Sustainable Energy Technology, Forskningsveien 1, 0373 Oslo, Norway*
[c] *Topsoe A/S, Haldor Topsøes Allé 1, DK-2800 Kgs., Lyngby, Denmark*

ARTICLE INFO

ABSTRACT

Stacking of solid oxide cells (SOC) requires that a robust and durable electrical contact is established between the cell and the interconnect. In this work, we present a contact layer solution for the SOC air side based on the concept of reactive oxidative bonding in which metallic Mn-Co and Mn-Cu particles are oxidized in-situ during stack initiation or operation to form robust well-conductive spinel oxides. The long-term (3000 h) stability of the new contact layers is evaluated by measuring the area specific resistance (ASR) during aging in air at 750 °C and 850 °C, and during thermal cycling. Both Mn-Co and Mn-Cu layers are found to be well compatible with a CeCo coated 441 steel interconnect material, and do not significantly contribute to the resistance across the stack element. The resistance is dominated by the coated steel.

1. Introduction

Stacking of solid oxide cells (SOC) is done to increase the power output or production capacity and requires that a robust and durable electrical contact is established between the cell and the interconnect [1–3]. To achieve this, contact layers are applied during the cell fabrication process before stack assembly. The contact layer should have a high electrical conductivity to aid with distributing the current across the cell. In addition, the contact layer material should have a thermal expansion coefficient (TEC) matching the other stack components and be mechanically robust and chemically compatible with the adjacent electrode and interconnect materials.

Perovskite oxides are a common choice for the contact material on the air/oxygen side of planar SOC stacks due to their high electrical conductivity and suitable TEC [4–6]. However, high temperatures (> 1100 °C) are required to properly sinter the perovskite oxides and adhere them to the interconnect. This heat treatment prior to stack assembly is not compatible with other SOC stack components such as the steel interconnect and the glass(-ceramic) seal [6]. Stack assembly is therefore performed well below 1000 °C, making the interface between the air electrode and the interconnect among the weakest and the most prone to loss of contact in state-of-the-art SOC stacks [7,8].

Poor electrical contact between the air electrode and the interconnect has been identified as one of the main reasons for the lower performance measured on stack level compared to single cells [2,3]. A break-down of the resistances in a Jülich stack of the F10 design operated at 650–800 °C showed that the La-Mn-Co-Cu-O-based air-side contact layer contributed to 40–50% of the total Ohmic resistance across the stack [9]. Improving the electrical contact between the air electrode and the interconnect is essential to improve the performance and durability of SOC stacks.

Several methods to improve bonding of the perovskite oxide contact layers have been investigated, including surface structuring to promote mechanical interlocking [10], and the use of sintering aids [11] or binders [12] to promote densification. Recently, promising results in terms of both mechanical robustness and electrical contact have been achieved by using CuMn metallic foam as the contact layer [13,14]. The foam was oxidized to a well-conductive spinel oxide during initial heat-up of the stack and formed a strong bond with both an LSC-CGO oxygen electrode and a coated interconnect [14].

An alternative way to fabricate spinel oxide contact layers is to use metal particles as the pre-cursors and utilize the concept of reactive oxidation to form the desired phase. Several combinations of different metals have been investigated for this purpose. Lu et al. [15] used Ni and

* Corresponding author at: Department of Energy Conversion and Storage, Technical University of Denmark, Anker Engelunds vej, KD-2800 Kgs., Lyngby, Denmark.
E-mail address: belma.talic@sintef.no (B. Talic).

Co metal particles to contact a $Ce_{0.02}Mn_{1.49}Co_{1.49}O_4$ coated 441 alloy with LSM and achieved a very low area specific resistance (ASR) of ~6 $m\Omega cm^2$ after 12000 h at 800 °C. Yu et al. [16] used alloyed Ni-Co-Fe (Kovar) particles as the contact layer and achieved a slightly higher ASR (~14 $m\Omega cm^2$ at 800 °C) between a Crofer 22 APU interconnect and a LSM cathode. Shong et al. [17] investigated 441/contact layer/441 assemblies with Ni-Co and Mn-Co metal particles as the contact layer and reported that the lowest ASR was achieved with Mn-Co (17 $m\Omega cm^2$ at 800 °C after 10000 h). Although these ASR values are encouraging, the typically low electrical conductivity of Ni-based spinel oxides may give rise to a high in-plane resistance [18].

We have recently reported on the fabrication of contact layers based on Mn-Co and Mn-Cu metallic precursors, mixed in the stoichiometric ratios to form $MnCo_2O_4$ and $Cu_{1.3}Mn_{1.7}O_4$, respectively [19,20]. These compositions were chosen as both oxides have an appreciable electrical conductivity (70 and 225 S/cm at 750 °C, respectively) and a TEC matching other typically used SOC materials (14.4 and 12.2 K^{-1} between 25 °C and 800 °C, respectively) [18,21]. Earlier investigations show that the fracture energy after sintering of the interconnect-contact layer interface was a factor of 6 higher with a Mn-Co based contact layer compared to conventional perovskite oxide contact materials such as (La,Sr)MnO₃ [14,19,20]. The fracture energy with a Mn-Cu based contact layer was even better – a factor of 6–13 higher compared to the conventional perovskite oxide based contact materials, depending on the type of interconnect steel (CeCo coated 441 or bare Crofer 22 H, respectively) [19,20].

Here, we evaluate the electrical conductivity and long-term stability of the Mn-Co and Mn-Cu based contact layers by measuring the ASR of a "stack element" comprising a steel interconnect, the contact layer and an air electrode. The ferritic stainless steel AISI 441 is chosen as the interconnect material, due to its lower cost compared to more specialized steel grades developed specifically for SOC interconnect application, such as Crofer 22 APU. Although previous work has revealed some challenges with the AISI 441 steel grade, namely the formation of insulating silica scales and poor oxide scale adhesion [22,23], promising results have been achieved when the 441 steel was coated with a thin layer of CeCo [24].

2. Experimental

The area specific resistance (ASR) was measured at 750 °C and 850 °C using a well-established set-up described in detail in Ref. [25]. An illustration of a stack element in this set-up is shown in Fig. 1a. By stacking several of these units together, the ASR as a function of time can be measured across multiple interfaces simultaneously. Here, the ASR was evaluated over five different configurations, schematically illustrated in Fig. 1b. At least two samples of the same type were evaluated.

The ferritic stainless steel AISI 441 in 0.3 mm thickness served as the

interconnect material. For the measurement at 750 °C, one side of the steel was coated with 10 nm Ce and 600 nm Co (Sandvik Materials – produced on the production line) while the other side was left uncoated. For the measurement at 850 °C, both sides of the steel were coated with CeCo (Sandvik Materials – produced with batch coater). The steel was cut into 20×40 mm^2 coupons and a Pt wire was spot welded along one of the shorter edges, to act as a voltage probe. For the single-side coated steel, the Pt-wire was welded to the uncoated side, while for the dual-side coated steel, the Pt-wire was welded on top of the (metallic) Co-coating.

Two different contact layers, Mn-Co and Mn-Cu, were screen printed onto a 20×20 mm^2 central area of the interconnect with a green thickness of ca. 0.4 mm. The pastes for screen printing were prepared using Mn (American Elements, 99.9%, APS ~ 2 µm), Co (Thermo Fisher, 99.8%, APS ~ 1.6 µm), and Cu (Thermo Fisher, 99%, APS ~ 2–3.5 µm) metal powders and a proprietary binder system. The powders were added in the stoichiometric amounts to upon oxidation form $MnCo_2O_4$ and $Cu_{1.3}Mn_{1.7}O_4$, respectively. The paste was dried at 90 °C for 1 h after screen printing to evaporate the solvent before assembly.

Bisque-sintered $La_{0.85}Sr_{0.1}Mn_{1.1}O_3$ (LSM) plates ($20\times20\times1$ mm^3) spray coated with a 50–60 µm layer of LSM and Co_3O_4 slurry mixture were used as current collection plates. The LSM plates were stacked between the interconnect coupons as illustrated in Fig. 1. Gold foils connected to gold wires were placed on the top and bottom of the stack to supply the current. A load of 7 kg was put on top of the stack. The stack was heated in stagnant air following a representative SOC stack heat-up profile used when employing glass-ceramic sealants, see reference [26]. This involved heating to 600 °C at 100 °C/h, holding for 1 h, heating to 700 °C at 100 °C/h, heating to 800 °C at 50 °C/h, holding for 1 h and finally cooling or heating (at 120 °C/h) to either 750 or 850 °C.

At 750 °C, the exposure was isothermal for the first 3000 h, followed by 50 thermal cycles. At 850 °C, the exposure was isothermal for 3588 h before carrying out 50 thermal cycles. The longer exposure in the latter case was due to three unscheduled thermal cycles during the isothermal exposure and because the stack had to be unmounted and remounted into the experimental setup due to maintenance during the test. Thermal cycling was in both cases carried out between the exposure temperature (750 or 850 °C) and 200 °C using a heating and cooling rate of 120 °C/h and a dwell time of 2 h at 750 or 850 °C, respectively. Thermal cycling was introduced to examine the mechanical robustness (interface adherence) of the stack elements after the growth of an oxide scale and after aging of a fully oxidized interface between the coupling components and the interconnect.

For all ASR measurements a current of 2 A was employed, corresponding to 0.5 A/cm^2 considering the nominal contact area between the steel interconnect and the LSM plate. The ASR was calculated according to Ohm's law, by measuring the voltage drop between the Pt-wire connected to the interconnect and a Pt-wire placed between two
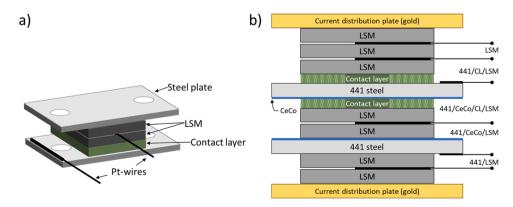

Fig. 1. Illustration of set-up used for measuring the area specific resistance. a) single repeating unit, b) overview of layer sequences for the different samples. CL = Contact Layer (Mn-Co or Mn-Cu). Note that the steel was coated on both sides for measurements at 850 °C.

LSM plates (see Fig. 1a):

$$ASR = \frac{\Delta V}{I} \bullet A$$

where ΔV is the voltage drop, I is the current and A is the nominal contact area (4 cm^2).

Microstructural characterization after the ASR measurement was performed using a scanning electron microscope (SEM, Zeiss Merlin) equipped with an energy dispersive X-ray spectrometer (EDS, Bruker). For this purpose, the whole ASR stack was embedded in epoxy and polished using SiC paper and diamonds in suspension to reveal the cross section. All EDS spectra were collected at an acceleration voltage of 15 kV.

3. Results

3.1. Isothermal aging at 750 °C

The ASR measured during isothermal aging in air at 750 °C is shown in Fig. 2. For clarity, only one curve representative for each interface is plotted. The maximum difference between two ASR measurements of equivalent samples was $\pm$ 3 mΩcm^2 for all but the 441/LSM interfaces, for which the scatter was greater ($\pm$ 16 mΩcm^2). An overview of the average ASR measured after 3000 h of aging and the degradations rates is given in Table 1. The degradation rates were calculated based on a linear fit of the ASR increase/decrease with time recorded during the last 500 h of isothermal aging.

The ASR of bare 441 steel contacted with LSM increased most rapidly during the first 500 h at 750 °C, after this, the degradation rate was slightly reduced and followed a linear trend with time ($+8.8$ mΩcm^2/ 1000 h). Coating the 441 steel with CeCo greatly reduced the degradation rate and resulted in a 2.6 times lower ASR after 3000 h at 750 °C. Applying a Mn-Cu contact layer on top of the CeCo coated 441 steel led to further decrease of the ASR, without influencing the degradation rate. The Mn-Co contact layer also reduced the ASR of CeCo coated 441 but in this case, the degradation rate was slightly increased compared to CeCo coated 441.

Applying the Mn-Co or Mn-Cu contact layers directly to the 441 (i.e., without a CeCo coating) also resulted in a lower and more stable ASR compared to bare 441. The ASR measured after 3000 h was comparable to that measured for CeCo coated 441, but the degradation rates with the contact layers was higher. To summarize, the overall best performance in terms of ASR and degradation rate was achieved with CeCo coated 441 and the Mn-Cu contact layer during steady state operation.

3.2. Thermal cycling 200–750 °C

During the 3000 h of isothermal aging at 750 °C the samples were exposed to two unplanned thermal cycles (at ca. 400 h and 2100 h), but

Table 1
ASR measured at 750 °C during 3000 h of isothermal aging and subsequent thermal cycling down to 200 °C. Average values and standard deviations of measurements of 2–4 interfaces of the same kind. The degradation rates were determined using linear regression.

Interface	Isothermal aging		Thermal cycling	
	ASR after 3000 h [mΩcm^2]	Degr. Rate[a] [mΩcm^2/ 1000 h]	ASR after 50 thermal cycles [mΩcm^2]	Degr. rate[b] [mΩcm^2/ cycle]
LSM	28	-0.7	29	-2.3
441/LSM	70 ± 16	9 ± 5	80 ± 29	14 ± 18
441/CeCo/ LSM	25 ± 3	-0.3 ± 0.2	24 ± 3	-0.8 ± 0.5
441/Mn-Co/LSM	25 ± 1	0.8 ± 0.4	24 ± 1	-0.2 ± 0.5
441/Mn-Cu/LSM	21 ± 1	-0.1 ± 0.2	20 ± 1	-0.5 ± 0.9
441/CeCo/ Mn-Co/ LSM	19 ± 2	0 ± 0.1	20 ± 1	-0.6 ± 0.1
441/CeCo/ Mn-Cu/ LSM	18 ± 1	-0.3 ± 0.3	17 ± 1	-0.7 ± 0.4

[a] Degradation rates extracted from the last 500 h of ASR measurement.
[b] Degradation rates calculated based on change in ASR per cycle, averaged over the 50 thermal cycles.

this did not have a noticeable influence on the ASR. After 3000 h of isothermal aging at 750 °C, the stack was intentionally exposed to 50 thermal cycles between 750 °C and 200 °C with a dwell of 2 h at 750 °C (cooling and heating at 120 °C/h). Fig. 3 shows the ASR measured at 750 °C for each cycle. The ASR measured after the 50th cycle and the average change in ASR per cycle is reported in Table 1.

For the uncoated 441 steel directly contacted to LSM, the degradation rate during thermal cycling increased ($+14$ mΩcm^2/1000 h) compared to the degradation rate measured during isothermal aging at 750 °C ($+8.8$ mΩcm^2/1000 h). For the samples with a CeCo coating and/or Mn-Co/Mn-Co contact layer the degradation rate during the thermal cycles was similar to or lower than measured during the last 500 h of isothermal aging at 750 °C, i.e. the thermal cycles did not accelerate the degradation. The decrease in degradation rate can be attributed to the LSM contacting components, for which the ASR decreases faster during thermal cycling than during isothermal aging.

3.3. Isothermal aging at 850 °C

Long-term aging at 850 °C was only possible with a CeCo coating on both sides of the steel, as bare 441 degraded too fast at this temperature. The first 200 h of ASR measurement on bare 441 at 850 °C is reported in the Supplementary Material. The ASR of 441 increased rapidly to above 200 mΩcm^2 after only 190 h, and it was therefore decided to terminate
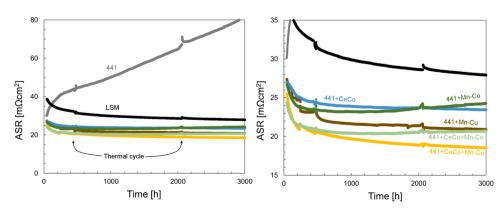

Fig. 2. ASR measured in air at 750 °C. Right side plot shows an excerpt of the ASR between 15 and 35 mΩcm^2.
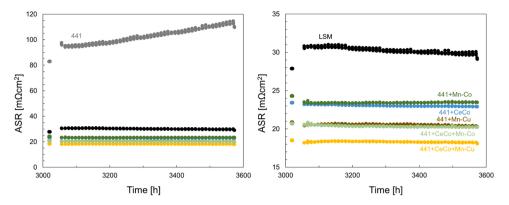
Fig. 3. ASR measured during thermal cycling between 750 °C and 200 °C. Only data recorded at 750 °C is plotted for each cycle for clarity. Right side plot shows an excerpt of the ASR between 15 and 35 mΩcm^2.

the measurement. Severe oxide scale spallation was observed in areas of the steel not covered by a contact layer or the LSM contacting plates.

The ASR measured for dual side CeCo coated 441 during aging at 850 °C is shown in Fig. 4. The temperature measured with a thermocouple placed close to the samples is also plotted, showing that the temperature decreased gradually by ca. 8 °C during the first 2790 h of the test and started to fluctuate after this, due to issues with the furnace.

The average ASR values recorded at the end of this period, and the degradation rate calculated from a linear fit during the 2000–2500 h period of the measurement are summarized in Table 2. The CeCo coated samples showed a much lower ASR compared to the bare steel and no visual signs of spallation were observed when removing the samples from the rig. Application of the contact layer reduced the ASR and furthermore resulted in less scatter between equivalent samples, as indicated by the standard deviations in Table 2. The lowest ASR and degradation rate was measured for CeCo coated 441 with a Mn-Cu contact layer, consistent with the results at 750 °C.

The samples were remounted in the rig after 2790 h and the test continued for an additional 800 h at 850 °C. During this period, the stack was exposed to one unplanned thermal cycle due to a power cut. The two thermal cycles caused a significant jump in the ASR of CeCo coated 441, followed by a period of relaxation where the ASR decreased

Table 2
ASR measured at 850 °C during isothermal aging and thermal cycling down to 200 °C. Average and standard deviation of measurement of 2–4 interfaces of the same kind. The degradation rates were determined using linear regression.

Interface	Isothermal aging		Thermal cycling	
	ASR after 2700 h [mΩcm^2]	Degr. Rate[a] [mΩcm^2/1000 h]	ASR after 50 thermal cycles [mΩcm^2]	Degr. rate[b] [mΩcm^2/cycle]
LSM	4.4	0.3	4.3	-1.6
441/CeCo/ LSM	25 ± 28	16 ± 22	52 ± 14	22 ± 13
441/CeCo/ Mn-Co/ LSM	16 ± 1	1.2 ± 0.5	19 ± 2	0.3 ± 0.8
441/CeCo/ Mn-Cu/ LSM	12 ± 1	-0.1 ± 0.5	12 ± 2	-0.8 ± 0.4

[a] Degradation rates extracted from measurements between 2000 and 2500 h at 850 °C.
[b] Degradation rates calculated based on change in ASR per cycle, averaged over the 50 thermal cycles.
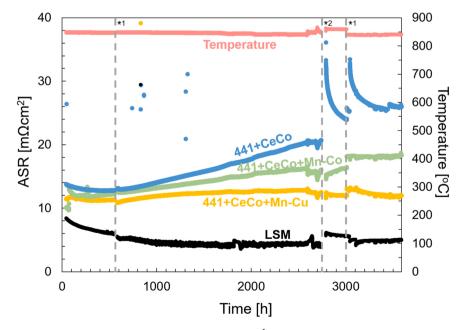

Fig. 4. ASR measured in air at ca. 850 °C. Stippled gray lines indicate thermal cycles. *1 indicates unscheduled thermal cycles, without controlled cooling, and *2 indicates thermal cycling with controlled heating and cooling and in combination with unmounting and remounting.

with time. In contrast, the thermal cycles had neglible influence on the ASR of samples with contact layers, which can be taken as an indication of more robust interfaces.

3.4. Thermal cycling 200–850 °C

After 3588 h at 850 °C, the stack was thermally cycled 50 times between 200 and 850 °C. The ASR recorded at 850 °C during these thermal cycles is plotted in Fig. 5. The ASR measured after the 50th cycle and the degradation rates in $m\Omega cm^2/1000$ h are reported in Table 2. The controlled thermal cycles had less influence on the ASR of CeCo coated 441 compared to the previous thermal cycles seen in Fig. 4. During the first 10 cycles, the ASR of CeCo coated 441 decreased with time. Following this, the ASR increased after each cycle, however, the increase with time is similar to the ASR increase measured during isothermal aging at 850 °C. For samples with the Mn-Co or Mn-Cu contact layer there is nearly no change to the ASR during thermal cycling, indicating a robust interface.

3.5. Microstructural analysis after ASR measurement at 750 °C

SEM cross sectional images of the Mn-Co and Mn-Cu contact layers after the ASR measurement at 750 °C are shown in Fig. 6. Both contact layers appear fully oxidized and partially densified after the long-term aging in air. The Mn-Co contact layer has a microstructure consisting of large (> 10 μm) and dense agglomerates surrounded by smaller ($<$ 1 μm) particles that appeared disconnected from each other and from the larger agglomerates. The Mn-Cu contact layer was fully dense in the 5–15 μm region closest to the steel and had a varying porosity further away. Overall, the density of the Mn-Cu contact layer was higher than the density of the Mn-Co contact layer.

In contrast to the two contact layers, the LSM+Co_3O_4 layer on the LSM contacting plate, which was also in the green state (i.e., not sintered) before the test, remained highly porous with almost no visible connectivity between the LSM or Co_3O_4 particles.

Higher magnification SEM images of the different interfaces, including non-coated and CeCo coated steel, are shown in Fig. 7. An oxide scale had formed on the steel surface of all samples after aging. On the bare 441 steel (Fig. 7a) the oxide scale consisted of an inner Cr_2O_3 layer and an outer $(Mn,Cr)_3O_4$ layer according to EDS analysis. The two oxides can be distinguished by their slightly different contrast in the backscatter electron (BSE) SEM image. On 441 steel with a CeCo coating (Fig. 7b) and CeCo coated 441 with a Mn-Co or Mn-Cu contact layer (Fig. 7c-d) the oxide scale consisted mainly of Cr_2O_3. Si-enrichment at the steel-oxide scale interface was detected by EDS on all samples (not shown), indicating the formation of a SiO_2 subscale.

The average thickness of the Cr-rich oxide scale for each sample is summarized in Table 3 and was determined by systematic measurement on multiple images. For the bare 441 steel, the oxide scale was partially damaged during sample preparation (epoxy casting and polishing) due to poor adhesion of the oxide scale to the steel surface, making it difficult to obtain an accurate measure for the oxide scale thickness.

For the CeCo coated sample, the 600 nm of Co was oxidized to an approx. 2 μm thick layer containing some closed porosity (Fig. 7b). For samples with a Mn-Co or Mn-Cu contact layer (Fig. 7c,d) the Co layer from the coating could not be clearly distinguished from the contact layer. The Ce from the CeCo coating was located on top of the Cr_2O_3 scale for the 441 +CeCo (Fig. 7b) and 441 +CeCo+Mn-Co (Fig. 7c) samples. For the 441 +CeCo+Mn-Cu sample (Fig. 7d), the Ce was found further into the contact layer, ca. 11 μm from the steel surface. The Mn-Cu contact layer was partially cracked after the aging, likely due to thermal cycling.

EDS mapping of CeCo-coated 441 with a Mn-Co or a Mn-Cu contact layer is shown in Fig. 8a and b, respectively. The EDS maps show complete interdiffusion between Co from the CeCo coating and the contact layers. The Mn-Co contact layer showed a homogeneous composition corresponding to $Co_{1.9}Mn_{1.1}O_4$ according to quantitative EDS analysis, while the Mn-Cu contact layer consisted of two distinguishable phases, with composition equal to Mn_2O_3 (purple areas) and $Mn_{1.8}Cu_{1.2}O_4$ (light blue areas) according to quantitative EDS analysis.

The interface between the oxide scale and the Mn-Co contact layer was sharp, and no Cr could be detected in the contact layer by EDS. In contrast, the interface between the oxide scale and the Mn-Cu contact layer was diffuse and the EDS map showed significant diffusion of Cr into the contact layer. The parts of the Mn-Cu contact layer containing Cr were visibly denser compared to the rest of the contact layer.

To determine how far Cr had diffused into the contact layer from the steel/oxide scale interface, multiple EDS linescans were recorded across
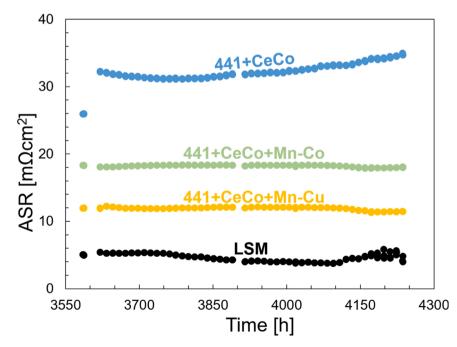

Fig. 5. ASR measured during thermal cycling between 850 °C and 200 °C. Only data recorded at 850 °C for each cycle is plotted for clarity.
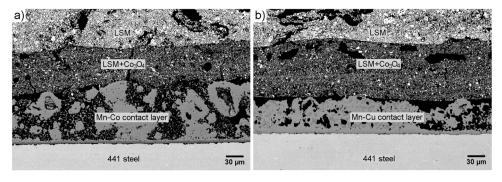
Fig. 6. Cross sectional SEM images of the a) Mn-Co and b) Mn-Cu contact layers after ASR measurement at 750 °C.
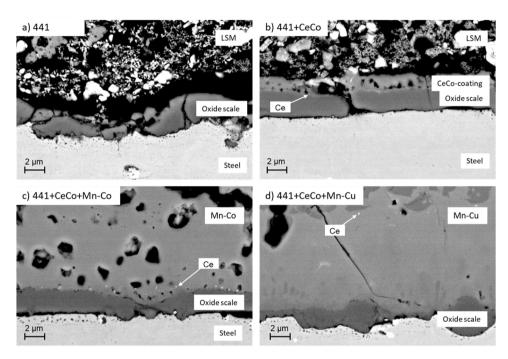

Fig. 7. SEM cross sections after ASR measurement at 750 °C. a) 441/LSM, b) 441/CeCo/LSM, c) 441/CeCo/Mn-Co/LSM, d) 441/CeCo/Mn-Cu/LSM.

Table 3

Measurement of oxide scale thickness and Cr diffusion distance for samples tested at 750 °C.

Interface	Cr_2O_3 thickness [μm]	Cr distance from steel surface [μm]
441/LSM	1.4 ± 1.0[a]	> 52
441/CeCo/LSM	2.1 ± 0.4	3.7 ± 0.2
441/CeCo/Mn-Co/ LSM	2.0 ± 0.1	3.3 ± 0.7
441/CeCo/Mn-Cu/ LSM	1.2 ± 0.5	11.8 ± 1.5
441/Mn-Co/LSM	3.5 ± 0.2	4.6 ± 0.9
441/Mn-Cu/LSM	1.1 ± 0.5	10.1 ± 2.3

[a] thickness measurement includes $(Mn,Cr)_3O_4$ scale and is not reliable due to cracks/delamination of sample

the interfaces of each sample and 5 wt% Cr was set as the threshold value. The results of this are summarized in Table 3. Without any coating or contact layer (441/LSM sample), Cr diffused far into the LSM contacting component (outside the analyzed area). In contrast, the CeCo coating as well as the Mn-Co and Mn-Cu contact layers acted as barriers against outward Cr diffusion. The most effective diffusion barrier, in terms of shortest Cr diffusion distance, was with the CeCo coating. The distance of Cr diffusion into the Mn-Cu contact layer correlates well with

the position of the Ce particles from the CeCo coating (see Fig. 7d).

3.6. Microstructural analysis after ASR measurement at 850 °C

SEM cross sectional images of the samples after ASR measurement at 850 °C are shown in Fig. 9. Oxidation at higher temperature led to the formation of a visibly thicker oxide scale on all three samples and the interface between the steel and the oxide scale appeared wavier compared to the samples tested at 750 °C. The CeCo-coated sample (Fig. 9a) was apparently in good contact with the LSM+Co₃O₄ layer of the LSM contacting plate, as particles from this layer were attached to the coating top surface. However, the contact was probably destroyed during sample preparation. The LSM+Co₃O₄ layer remained highly porous even after aging at 850 °C similar to aging at 750 °C.

The Mn-Co contact layer (Fig. 9b) appeared much denser after aging at 850 °C compared to 750 °C. Some porosity remained in the contact layer, but there were hardly any of the smaller particles visible that had been observed at 750 °C. The Mn-Cu contact layer had similar morphology after aging at 850 °C as at 750 °C, that is, the contact layer was very dense in close proximity to the steel and appeared with large pores further away from the steel surface. The average oxide scale thickness of the different samples is summarized in Table 4. The standard deviations were larger for the oxide scale thickness of samples exposed to 850 °C than samples exposed to 750 °C. This can be
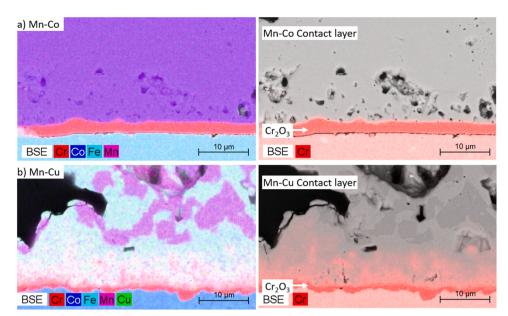
Fig. 8. SEM images of samples tested at 750 °C overlaid with EDS maps. a) 441/CeCo/Mn-Co/LSM interface, b) 441/CeCo/Mn-Cu/LSM interface.
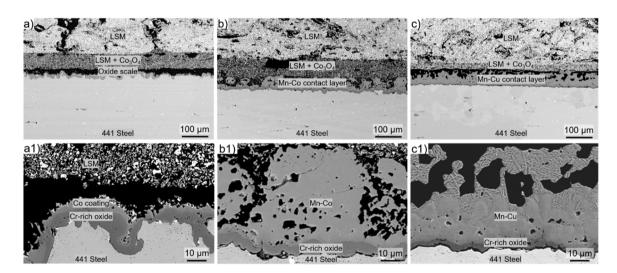

Fig. 9. SEM cross sections after ASR measurements at 850 °C. a) and a1) 441/CeCo/LSM, b) and b1) 441/CeCo/Mn-Co/LSM, c) and c1) 441/CeCo/Mn-Cu/LSM.

Table 4
Measurement of oxide scale thickness and Cr diffusion distance for samples tested at 850 °C.

Interface	Cr$_2$O$_3$ thickness [μm][a]	Cr distance from steel surface [μm][a]
441/CeCo/LSM	4.0 ± 1.9	[b]
441/CeCo/Mn-Co/ LSM	5.3 ± 1.0	10.4 ± 2.0
441/CeCo/Mn-Cu/ LSM	2.5 ± 0.7	24.3 ± 3.8

[a] The waviness of the thermally grown oxide scale gives the high standard deviations for both the oxide scale thickness and the Cr diffusion depth.
[b] Due to the detachment between the oxide scale and LSM the Cr distance from the steel/oxide interface could not be determined.

explained by the increased waviness of the oxide scales of samples exposed to the higher temperature.

Fig. 10 shows EDS mapping of CeCo-coated 441 with a Mn-Co or a Mn-Cu contact layer exposed at 850 °C. The contact layers appeared similar as after aging at lower temperature, i.e. Mn-Co had a

homogeneous composition, while Mn-Cu was composed of two phases. The EDS maps also show that aging at 850 °C resulted in Cr diffusing further into the contact layers than aging at 750 °C, see Table 4. For CeCo-coated 441 exposed at 850 °C the Cr diffusion length could not be accurately determined due to the large gap between the oxide scales and the LSM layer, and the high porosity of the LSM layer. These factors led to a low signal-to-noise ratio. However, EDX point analysis of the Co oxide layer on the contact plate showed a high Cr content of around 25 wt%, whereas the Cr content in the LSM layer, and as close to the LSM-Co-oxide interface as possible, was below 1 wt%. This suggests that the Cr diffused into the Co-oxide spinel but did not diffuse further into the LSM. Similar to result at 750 °C, at 850 °C, Cr diffused much farther into the Mn-Cu contact layer than into the Mn-Co contact layer.

4. Discussion

4.1. Isothermal ASR measurements

The ASR of the interconnect and contact layer is a function of the thickness and conductivity of each layer, any reaction products formed
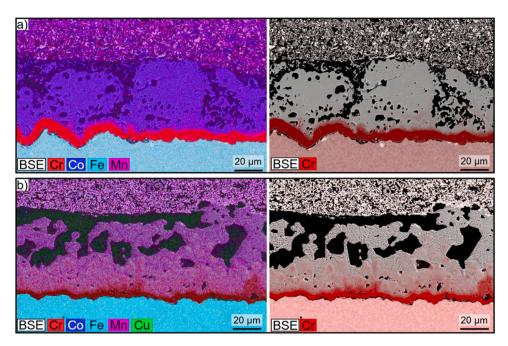
Fig. 10. SEM images of samples tested at 850 °C overlaid with EDS maps. a) 441/CeCo/Mn-Co/LSM interface, b) 441/CeCo/Mn-Cu/LSM interface.

at the interfaces, and the actual contact area. In this work, the ASR was calculated based on the nominal contact area (4 cm^2), which may differ from the actual contact area due to slight misalignment between the components, or differences in creep and sintering of the materials. Additionally, different studies have employed different contacting components and loads during the measurement leading to a further complication of comparing the recorded ASR values in this work to literature values. These factors make it difficult to compare ASR results across literature. The measurement set-up used in this work was designed to be as representative as possible of the interfaces found on the oxygen side of a SOC stack, by utilizing LSM-based contacting components. Although the absolute ASR values will likely be different in a real SOC stack, the recorded changes in ASR with time are valuable for comparing different combinations of steel, coating, and contact layer, and identifying the most promising solution.

The measurements showed rapid increase in ASR with time for the uncoated 441 steel, exceeding 50 mΩcm^2 already after 1000 h of aging at 750 °C. The rapid increase in the ASR of uncoated 441 steel is consistent with previous measurements and can be attributed to the growth of a poorly conductive Cr$_2$O$_3$ scale or even an insulating layer of SiO$_2$ on the bare 441 steel [22,27]. The growth of Cr$_2$O$_3$ typically follows a parabolic trend while here, the ASR of 441 was found to increase linearly with time. This is likely because the ASR is influenced not only by the oxide scale thickness, but also its conductivity, which may change with time due to interdiffusion between the layers and doping of the oxide scale. At 850 °C the ASR of 441 increased even faster to above 200 mΩcm^2 after only 190 h and the steel showed signs of oxide scale spallation. This is consistent with results from literature, showing oxide scale spallation on bare 441 steel after only 100 h at 850 °C [28].

The ASR of 441 at both 750 °C and 850 °C was greatly reduced by the application of a CeCo coating, which indicates a reduced growth rate and/or improved electrical conductivity of the thermally grown oxide scale. Although the conductivity of the oxidized coating is modest (6.7 S/cm at 800 °C for Co$_3$O$_4$ [18]), the coating layer is relatively thin and therefore likely has a minimal contribution to the ASR relative to the oxide scale (0.1–0.01 S/cm for Cr$_2$O$_3$ [29,30] and 10^{-10}-10^{-8} S/cm for SiO$_2$ at 750 °C [31]). This has been verified experimentally by previous ASR measurements [27].

The ASR of CeCo coated 441 was further reduced by application of a Mn-Co or Mn-Cu contact layer. Although the contact layers were much

thicker (50–100 μm) than the coating and the thermally grown oxide scale, their higher electrical conductivity (70 S/cm for MnCo$_2$O$_4$ ([21] and 225 S/cm for Cu$_{1.3}$Mn$_{1.7}$O$_4$ [18]) makes it reasonable to assume that the contact layers, similar to the coating, do not contribute significantly to the cross-plane resistance.

Screen printing a Mn-Co or Mn-Cu contact layer directly on 441 steel resulted in nearly the same improvement in ASR as coating the steel with CeCo. This is not surprising considering that the oxidized form of the contact layers, i.e. MnCo$_2$O$_4$ and Cu$_{1.3}$Mn$_{1.7}$O$_4$, have been shown to provide good protection when applied as interconnect coatings [32–34]. Nevertheless, the best performance in terms of ASR after 3000 h and the lowest degradation rate with time was achieved by combining the CeCo coating with the Mn-Cu or Mn-Co contact layer. The Co from the coating diffused into the contact layers and could not be distinguished as a separate layer after exposure regardless of exposure temperature. The interdiffusion likely happened rapidly, as the coating/contact layer interface was metallic initially and both the coating and the contact layers oxidize to form a spinel structure. Thus, the improved ASR when combining the contact layers with the CeCo coating is likely due to the addition of Ce, a reactive element that has been earlier shown to be effective in reducing the oxidation rate of ferritic stainless steels [35,36]. The CeCo coating is furthermore known to be beneficial for reducing the release of poisonous Cr(VI)-species from the interconnect that cause degradation of the oxygen electrode [37]. This additional benefit of the CeCo coating is important for stack applications, where the interconnect will be corrugated and the contact layer most likely applied only to the contact points between the interconnect and the cell.

In the present work, the overall trend in oxide scale thicknesses correlated well with the trend in ASR measured for the coated samples. That is, the samples having a thinner oxide scale also showed a lower ASR. The thinnest oxide scale was measured for a Mn-Cu contact layer on CeCo coated 441. This further supports the argument that the thermally grown oxide scale (i.e., Cr$_2$O$_3$ and SiO$_2$) was the main contributor to the ASR and that the electrical conductivity of the oxidized contact layers were sufficiently high not to influence the ASR. Overall, the ASR measured at 850 °C was lower than that measured at 750 °C, while the degradation rates were higher. This reflects the increase in electrical conductivity of the semiconducting oxides and the increased growth rate of the oxide scale at higher temperature [42]. The former will lower the ASR, while the latter will result in a faster increase in the ASR with time.

For nearly all samples, the ASR decreased during the initial 1000–2000 h of aging at 750 °C. This can be attributed to an improvement of the true contact area and improved conductance of the green and only mildly sintered layers. The former is primarily related to creep and sintering of the LSM contacting plates [38], which were pre-sintered under mild conditions and coated with a LSM/Co$_3$O$_4$ layer. As seen in Fig. 2, the ASR measured across a single LSM plate continued to decrease over the entire duration of the measurement at 750 °C. Due to the increased sintering activity/creep rate at higher temperature, the ASR of LSM measured at 850 °C was lower and reached a nearly constant value after only 1000 h. Similarly, the period during which the ASR of the other samples decreased was shorter at 850 °C (< 500 h) than at 750 °C. Thus, the contribution from the LSM plate was smaller at 850 °C compared to 750 °C, both in terms of resistance and change in ASR with time. This is likely due to faster creep/sintering of the initially porous LSM at higher temperatures.

4.2. Effect of thermal cycling

For the uncoated 441 steel directly contacted to LSM, the degradation rate during thermal cycling was increased (+13.5 mΩcm^2/1000 h) compared to the degradation rate during isothermal aging at 750 °C (+8.8 mΩcm^2/1000 h). The increased degradation during thermal cycling was likely caused by a loss in contact area between the steel and the LSM contacting plate, due to partial oxide scale spallation. Poor oxide scale adhesion is a known challenge with the 441 steel, and (partial) spallation may occur during thermal cycling due to the stresses that develop from the TEC mismatch between the steel and the oxide scale [39,40].

For samples where the steel was coated with CeCo and/or a contact layer, the degradation during thermal cycling was the same as or lower than during isothermal aging at 750 °C. The decrease in degradation rate per 1000 h could be an artifact caused by a shorter time spent at 750 °C for thermal cycling than for isothermal aging; i.e. the 1000 h for the former case also includes cooling down to 200 °C and heating up again. Thus, the real degradation rate could be the same for both cases. As it is impossible to define an accurate cut-off temperature below which no oxidation occurs, no cleaned degradation rate was calculated (note that degradation rates reported in Tables 1 and 2 are per thermal cycle). For samples tested at 850 °C the degradation rate during thermal cycling was higher for CeCo coated 441 compared to samples with both the CeCo coating and the Mn-Co or Mn-Cu contact layer. The stable performance during thermal cycling indicates a good TEC match and satisfactory bonding between the different layers (steel/coating/contact layer). The results here are supported by the high values of interface toughness for the steel/441/contact layer interface reported in [20,41]. The occasional cracks in the contact layer (as seen in Fig. 7d) did not apparently influence the ASR.

4.3. Comparison between Mn-Co and Mn-Cu contact layers

Overall, the best results in terms of a low ASR and a slow degradation rate of ASR were achieved with the Mn-Cu contact layer. A prominent difference between the two contact layers is their reactivity with the thermally grown oxide scale. The Mn-Co contact layer showed excellent Cr retention capability at 750 °C, with essentially no Cr diffusion into the contact layer after more than 3000 h of aging. The interface between the Cr$_2$O$_3$ scale and the contact layer was distinct and decorated by Ce from the CeCo coating. Assuming Ce can be treated as an inert marker, this is further evidence of limited interdiffusion between the oxide scale and the Mn-Co contact layer. After aging at 850 °C there is some Cr found in the Mn-Co contact layer, up to 10.4 ± 2 µm from the steel Cr$_2$O$_3$ scale interface. However, the amount and diffusion distance are still significantly decreased compared to the Mn-Cu contact layer.

The Mn-Cu contact layer was less efficient at mitigating Cr outward diffusion and Cr was found far into the contact layer (up to 15 µm from

steel) even after aging at 750 °C. The interface between the Cr$_2$O$_3$ scale and the Mn-Cu contact layer was much more diffuse than with the Mn-Co contact layer. Ce from the CeCo coating was found some distance into the Mn-Cu contact layer, corresponding well with the diffusion distance of Cr. If Ce is treated as an inert marker for the original steel/coating interface, these results indicate that Mn and Cu are diffusing towards the Cr$_2$O$_3$ scale rather than Cr diffusing outwards. Interdiffusion and reaction between the oxide scale and the Mn-Cu contact layer is a likely reason for the thinner oxide scale measured on samples with a Mn-Cu contact layer compared to samples with a Mn-Co contact layer. While this is beneficial for lowering the ASR, it may become a concern for even longer-term operation, as Cr may diffuse all the way to the contact layer surface, where it can volatilize and cause poisoning of the oxygen electrode. Additionally, the decreased Cr$_2$O$_3$ scale thickness for the Mn-Cu contact layer should lead to increased Cr consumption, which accelerates Cr depletion of the steel and, with that, also accelerates the formation of break-away corrosion for the Mn-Cu case.

After long-term aging, the Mn-Cu contact layer consisted of two distinguishable phases, Mn$_2$O$_3$ and Mn$_{1.8}$Cu$_{1.2}$O$_4$. This is consistent with the Mn-Cu-oxide phase diagram reported by Broemme and Brabers [43], which shows that the Mn/Cu ratio used in this work should form Mn$_2$O$_3$ in addition to a spinel oxide phase at low temperatures, while a single phase spinel oxide is stabilized between 600 and 750 °C. Since the ASR samples were slowly cooled to room temperature after the long-term test, it is possible that the Mn$_2$O$_3$ precipitated during cooling. As no increase in degradation was observed during thermal cycling of samples with the Mn-Cu contact layer, the presence of two phases does not appear to have any apparent detrimental effects on the performance.

5. Conclusions

Mn-Co and Mn-Cu have been evaluated as contact materials in combination with bare and CeCo coated AISI441 steel by measuring the area specific resistance (ASR) during long-term (3000 h) aging at 750 °C and 850 °C and during thermal cycling.

The ASR for all samples was found to be dominated by the oxide scale thermally grown on the 441 steel. Application of a CeCo coating onto the bare steel significantly reduced the ASR and applying the Mn-Co or Mn-Cu contact layers led to a further decrease in ASR. The lowest ASR was measured for CeCo coated 441 with a Mn-Cu contact layer, at both 750 °C and 850 °C. Both contact layers greatly improved performance during thermal cycling compared to the CeCo coated 441 reference, resulting in negligible increase in ASR over 50 cycles. The stable performance during thermal cycling indicates a good TEC match and satisfactory bonding between the different layers.

Post-test analysis showed that the Mn-Co contact layer acts as a barrier against outward Cr diffusion from the steel, but that the CeCo coating provided even more efficient protection. The Mn-Cu contact layer increased the diffusion of Cr from the steel into the contact layer, also when the steel was coated with CeCo. This behavior may be of concern for long-term operation of stacks with the Mn-Cu contact layer, if the Cr depletes from the steel and/or eventually reaches the surface of the contact layer and volatilizes.

Declaration of Competing Interest

The authors declare that they have no known competing financial interests or personal relationships that could have appeared to influence the work reported in this paper.

Acknowledgments

Innovation program, Hydrogen Europe and Hydrogen Europe Research.

Appendix A. Supporting information

Supplementary data associated with this article can be found in the online version at doi:10.1016/j.jeurceramsoc.2023.10.055.

References

[1] S.P. Jiang, J.G. Love, L. Apateanu, Effect of contact between electrode and current collector on the performance of solid oxide fuel cells, Solid State Ion.-. 160 (2003) 15–26, https://doi.org/10.1016/S0167-2738(03)00127-9.

[2] T. Dey, P.C. Ghosh, D. Singdeo, M. Bose, R.N. Basu, Diagnosis of scale up issues associated with planar solid oxide fuel cells, Int. J. Hydrog. Energy 36 (2011) 9967–9976, https://doi.org/10.1016/j.ijhydene.2011.05.052.

[3] W. Wu, G.L. Wang, W.B. Guan, Y.F. Zhen, W.G. Wang, Effect of contact method between interconnects and electrodes on area specific resistance in planar solid oxide fuel cells, Fuel Cells 13 (2013) 743–750, https://doi.org/10.1002/fuce.201300028.

[4] J.H. Zhu, H. Ghezel-Ayagh, Cathode-side electrical contact and contact materials for solid oxide fuel cell stacking: a review, Int. J. Hydrog. Energy (2017), https://doi.org/10.1016/j.ijhydene.2017.08.005.

[5] X. Montero, F. Tietz, D. Stöver, M. Cassir, I. Villarreal, Comparative study of perovskites as cathode contact materials between an La0.8Sr0.2FeO3 cathode and a Crofer22APU interconnect in solid oxide fuel cells, J. Power Sources 188 (2009) 148–155, https://doi.org/10.1016/j.jpowsour.2008.11.083.

[6] M.C. Tucker, L. Cheng, L.C. DeJonghe, Selection of cathode contact materials for solid oxide fuel cells, J. Power Sources 196 (2011) 8313–8322, https://doi.org/10.1016/j.jpowsour.2011.06.044.

[7] D.N. Boccaccini, O. Sevecek, H.L. Frandsen, I. Dlouhy, S. Molin, B. Charlas, J. Hjelm, M. Cannio, P.V. Hendriksen, Determination of the bonding strength in solid oxide fuel cells' interfaces by Schwickerath crack initiation test, J. Eur. Ceram. Soc. 37 (2017) 3565–3578, https://doi.org/10.1016/j.jeurceramsoc.2017.04.018.

[8] N.H. Menzler, P. Batfalsky, S. Groß, V. Shemet, F. Tietz, Post-test characterization of an SOFC short-stack after 17,000 hours of steady operation, ECS Trans. 35 (2011) 195–206, https://doi.org/10.1149/1.3569994.

[9] D. Kennouche, Q. Fang, L. Blum, D. Stolten, Analysis of the cathode electrical contact in SOFC stacks, J. Electrochem. Soc. 165 (2018) F677–F683, https://doi.org/10.1149/2.0761809jes.

[10] Y.-S. Chou, J.F. Bonnett, J.W. Stevenson, Novel approach to strengthening ceramic cathode contact and validation in a generic stack test fixture, ECS Trans. 78 (2017) 1713–1720, https://doi.org/10.1149/07801.1713ecst.

[11] W.-J. Shong, C.-K. Liu, C.-W. Lu, S.-H. Wu, R.-Y. Lee, Characteristics of La0.6Sr0.4Co0.2Fe0.8O3–Cu2O mixture as a contact material in SOFC stacks, Int. J. Hydrog. Energy 42 (2017) 1170–1180, https://doi.org/10.1016/j.ijhydene.2016.08.211.

[12] M.C. Tucker, L.C. DeJonghe, V. García-Negrón, R. Trejo, E. Lara-Curzio, Mechanical and electrochemical performance of composite cathode contact materials for solid oxide fuel cells, J. Power Sources 239 (2013) 315–320, https://doi.org/10.1016/j.jpowsour.2013.03.130.

[13] P. Zielke, A.C. Wulff, X. Sun, S.H. Jensen, R. Kiebach, H.L. Frandsen, P. Norby, A. Hagen, Investigation of a spinel-forming Cu-Mn foam as an oxygen electrode contact material in a solid oxide cell single repeating unit, Fuel Cells 17 (2017) 730–734, https://doi.org/10.1002/fuce.201700005.

[14] L. Han, B. Talic, K. Kwok, P.V. Hendriksen, H.L. Frandsen, Interface fracture energy of contact layers in a solid oxide cell stack, ACS Appl. Energy Mater. (2020), https://doi.org/10.1021/acsaem.9b02026.

[15] Z. Lu, G. Xia, J.D. Templeton, X. Li, Z. Nie, Z. Yang, J.W. Stevenson, Development of Ni1-xCoxO as the cathode/interconnect contact for solid oxide fuel cells, Electrochem. Commun. 13 (2011) 642–645, https://doi.org/10.1016/j.elecom.2011.03.034.

[16] Y.T. Yu, J.H. Zhu, B.L. Bates, Effect of precursor materials on the performance of the NiFe2O4-based spinel layer for SOFC cathode-side contact application, Solid State Ion.-. 324 (2018) 40–48, https://doi.org/10.1016/j.ssi.2018.05.030.

[17] W.-J. Shong, C.-K. Liu, W.-H. Shiu, R.-Y. Lee, Characteristics of Mn-Co and Ni-Co metal powders mixed with oxides as cathode contact materials for SOFC, Int. J. Hydrog. Energy 44 (2019) 4317–4331, https://doi.org/10.1016/j.ijhydene.2018.12.146.

[18] A. Petric, H. Ling, Electrical conductivity and thermal expansion of spinels at elevated temperatures, J. Am. Ceram. Soc. 90 (2007) 1515–1520, https://doi.org/10.1111/j.1551-2916.2007.01522.x.

[19] I. Ritucci, B. Talic, R. Kiebach, H.L. Frandsen, High toughness well conducting contact layers for solid oxide cell stacks by reactive oxidative bonding, J. Eur. Ceram. Soc. (2020), https://doi.org/10.1016/j.jeurceramsoc.2020.11.021.

[20] Y.A. Farzin, I. Ritucci, B. Talic, R. Kiebach, H.L. Frandsen, Fracture toughness of reactive bonded Co–Mn and Cu–Mn contact layers after long-term aging, Ceram. Int. 48 (2022) 20699–20711, https://doi.org/10.1016/j.ceramint.2022.04.050.

[21] B. Talic, P.V. Hendriksen, K. Wiik, H.L. Lein, Thermal expansion and electrical conductivity of Fe and Cu doped MnCo2O4 spinel, Solid State Ion.-. 326 (2018) 90–99, https://doi.org/10.1016/j.ssi.2018.09.018.

[22] Z. Yang, G.-G. Xia, C.-M. Wang, Z. Nie, J. Templeton, J.W. Stevenson, P. Singh, Investigation of iron–chromium–niobium–titanium ferritic stainless steel for solid oxide fuel cell interconnect applications, J. Power Sources 183 (2008) 660–667, https://doi.org/10.1016/j.jpowsour.2008.05.037.

[23] B. Talic, V. Venkatachalam, P.V. Hendriksen, R. Kiebach, Comparison of MnCo2O4 coated Crofer 22H, 441, 430 as interconnects for intermediate-temperature solid oxide fuel cell stacks, J. Alloy. Compd. (2019), 153229, https://doi.org/10.1016/j.jallcom.2019.153229.

[24] J.G. Grolig, J. Froitzheim, J.-E. Svensson, Coated stainless steel 441 as interconnect material for solid oxide fuel cells: evolution of electrical properties, J. Power Sources 284 (2015) 321–327, https://doi.org/10.1016/j.jpowsour.2015.03.029.

[25] S. Molin, P. Jasinski, L. Mikkelsen, W. Zhang, M. Chen, P.V. Hendriksen, Low temperature processed MnCo2O4 and MnCo1.8Fe0.2O4 as effective protective coatings for solid oxide fuel cell interconnects at 750 °C, J. Power Sources 336 (2016) 408–418, https://doi.org/10.1016/j.jpowsour.2016.11.011.

[26] I. Ritucci, K. Agersted, P. Zielke, A.C. Wulff, P. Khajavi, F. Smeacetto, A.G. Sabato, R. Kiebach, A Ba-free sealing glass with a high coefficient of thermal expansion and excellent interface stability optimized for SOFC/SOEC stack applications, Int. J. Appl. Ceram. Technol. (2018) 1011–1022, https://doi.org/10.1111/ijac.12853@10.1111/(ISSN)1744-7402.mcare(vi).

[27] C. Goebel, A.G. Fefekos, J.-E. Svensson, J. Froitzheim, Does the conductivity of interconnect coatings matter for solid oxide fuel cell applications? J. Power Sources 383 (2018) 110–114, https://doi.org/10.1016/j.jpowsour.2018.02.060.

[28] J.G. Grolig, J. Froitzheim, J.-E. Svensson, Coated stainless steel 441 as interconnect material for solid oxide fuel cells: oxidation performance and chromium evaporation, J. Power Sources 248 (2014) 1007–1013, https://doi.org/10.1016/j.jpowsour.2013.08.089.

[29] A. Holt, P. Kofstad, Electrical conductivity and defect structure of Cr_2O_3. II. Reduced temperatures (< 1000 °C), Solid State Ion.-. 69 (1994) 137–143.

[30] J.A. Crawford, R.W. Vest, Electrical conductivity of single-crystal Cr_2O_3, J. Appl. Phys. 35 (1964) 2413, https://doi.org/10.1063/1.1702871.

[31] J.K. Srivastava, M. Prasad, J.B. Wagner, Electrical conductivity of silicon dioxide thermally grown on silicon, J. Electrochem. Soc. 132 (1985) 955–963, https://doi.org/10.1149/1.2113993.

[32] B. Talic, S. Molin, K. Wiik, P.V. Hendriksen, H.L. Lein, Comparison of iron and copper doped manganese cobalt spinel oxides as protective coatings for solid oxide fuel cell interconnects, J. Power Sources 372 (2017) 145–156, https://doi.org/10.1016/j.jpowsour.2017.10.060.

[33] J.W. Stevenson, Z.G. Yang, G.G. Xia, Z. Nie, J.D. Templeton, Long-term oxidation behavior of spinel-coated ferritic stainless steel for solid oxide fuel cell interconnect applications, J. Power Sources 231 (2013) 256–263, https://doi.org/10.1016/j.jpowsour.2013.01.033.

[34] P. Wei, M.R. Bateni, A. Petric, Conversion of copper and manganese metallic films to spinel coating, J. Mater. Sci. 47 (2012) 5205–5215, https://doi.org/10.1007/s10853-012-6404-4.

[35] M. Sattari, R. Sachitanand, J. Froitzheim, J.E. Svensson, T. Jonsson, The effect of Ce on the high temperature oxidation properties of a Fe–22%Cr steel: microstructural investigation and EELS analysis, Mater. High. Temp. 32 (2015) 118–122, https://doi.org/10.1179/0960340914Z.00000000084.

[36] A. Harthøj, T. Holt, P. Møller, Oxidation behaviour and electrical properties of cobalt/cerium oxide composite coatings for solid oxide fuel cell interconnects, J. Power Sources 281 (2015) 227–237, https://doi.org/10.1016/j.jpowsour.2015.01.128.

[37] J. Froitzheim, S. Canovic, M. Nikumaa, R. Sachitanand, L.G. Johansson, J.E. Svensson, Long term study of Cr evaporation and high temperature corrosion behaviour of Co coated ferritic steel for solid oxide fuel cell interconnects, J. Power Sources 220 (2012) 217–227, https://doi.org/10.1016/j.jpowsour.2012.06.092.

[38] S. Koch, P.V. Hendriksen, Contact resistance at ceramic interfaces and its dependence on mechanical load, Solid State Ion.-. 168 (2004) 1–11, https://doi.org/10.1016/j.ssi.2004.01.010.

[39] M. Schütze, Mechanical properties of oxide scales, Oxid. Met. 44 (1995) 29–61, https://doi.org/10.1007/BF01046722.

[40] W. Liu, X. Sun, E. Stephens, M. Khaleel, Interfacial shear strength of oxide scale and SS 441 substrate, Metall. Mater. Trans. A. 42 (2011) 1222–1228, https://doi.org/10.1007/s11661-010-0537-3.

[41] H.L. Frandsen, I. Ritucci, P. Khajavi, B. Talic, R. Kiebach, P.V. Hendriksen, Enhancing the robustness of brittle solid oxide cell stack components, ECS Trans. 91 (2019) 2201–2211, https://doi.org/10.1149/09101.2201ecst.

[42] P. Kofstad, High Temperature Corrosion, 1988.

[43] A.D.D. Broemme, V.A.M. Brabers, Preparation and properties of copper- and manganese containing mixed oxides, Solid State Ion.-. 16 (1985) 171–177, https://doi.org/10.1016/0167-2738(85)90040-2.